16TH EUROPEAN CONFERENCE ON EARTHQUAKE ENGINEERING THESSALONIKI 18 - 21 JUNE 2018

VIBRATORY COMPACTION LOAD EFFECTS ON MSE WALLS

Hamzeh AHMADI[1], Adam BEZUIJEN[2]

ABSTRACT

This paper presents the behavior of MSE walls under a localized vibratory roller compactor load in full scale model tests and the results of numerical simulation of these tests. Two full scale tests were only different in the flexibility of the facing elements (with full rigid or full flexible face). The effect of the vibratory plate compactor used during the backfill construction step to compact the soil layers is also considered in this study. A number of different strategies are available to simulate placement and compaction of soil layers; a single load-unload stress cycle and two equal distributed loads in top and bottom of each soil layer. The results of numerical analysis (Plaxis 2D) were compared with the full-scale test results in which the vertical and horizontal earth pressures, strains on reinforcement layers and consequently maximum tensile force on reinforcement layers were measured. Both in the tests and in the numerical analysis, the compaction has a significant effect on the magnitude of construction-induced horizontal earth pressure of MSE walls. In both the experimental tests and the numerical analysis, a big difference was found between the lateral earth pressure coefficient compared with the calculated Rankine at-rest and active earth pressure coefficients.

Keywords: Full scale model tests; MSE wall; Vibratory compaction load; Dynamic load; Numerical analysis.

1. INTRODUCTION

Vibratory rollers and plate compactors have been used successfully in many projects for compacting the granular soil (Toombes, 1969). The frequency and deadweight of vibratory rollers must be suited to the soil material being compacted. For instance, heavyweight rollers with low-frequency vibrations are used to compact gravel; light to medium-weight rollers with high-frequency vibrations are used for sands (Bell, 1993). Monitoring of the compaction obtained by plate compaction and roller vibration have been studied by Kröber et al. (2001); Anderegg and Kaufmann (2004); Mooney and Rinehart (2007).

Bathurst et al. (2009) reported that compaction has a significant effect on the magnitude of construction-induced outward wall deformation and the horizontal earth load at the end of construction of GRS walls. Tatsuoka et al. (1997) and Uchimura et al. (2003) proposed the pre-loaded and pre-stressed reinforced soil method in abutment of geogrid. The transient and long-term residual deformations measured in the wall after pre-loading were reported to be very small. Ehrlich and Mitchell (1995) indicated that the induced stress due to soil compaction may represent a kind of pre-stressing and reduce lateral displacement after wall construction.

As shown in Figure 1, a number of different strategies are available to simulate placement and compaction of soil layers in a numerical simulation. Some researchers considered the compaction effect by only applying a static surcharge (8 kPa for the light and 16 kPa for the heavy compactor) over the soil layers (Gotteland et al. 1996; Hatami and Bathurst (2005, 2006); Huang et al. 2009).

[1]PhD student, Ghent University, Department of Civil Engineering, Laboratory of Geotechnics, Technologiepark 905, B-9052 Gent, Belgium, hamzeh.ahmadi@ugent.be.
[2]Professor, Ghent University, Department of Civil Engineering, Laboratory of Geotechnics, Technologiepark 905, B-9052 Gent, Belgium and senior specialist Deltares, Delft the Netherlands, adam.bezuijen@ugent.be.

More recently it was suggested to apply the same surcharges over and under the soil layers (Ehrlich and Mirmoradi (2013, 2014) and Riccio et al. 2014). The considered magnitude of the compaction load for a vibratory tamper was 64 kPa in these studies. The differences between these two compaction models are the magnitude and the way for considering the compaction load influence in depth and for layers underneath.

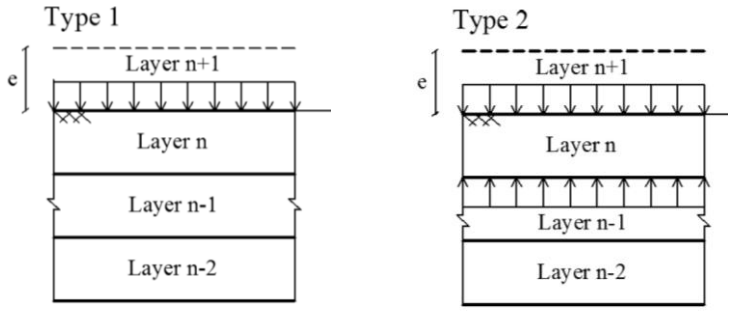

Figure 1. Modeling of the vertical stress load–unload cycles during the compaction of the backfill soil layer; (a) type 1, (b) type 2, (Mirmoradi and Ehrlich, 2014).

For numerical analysis in this study, two different strategies were used to model the compaction process with the vibratory plate. A single load-unload stress cycle with distributed load of 16 kPa at the top of each backfill soil layer (similar to Hatami and Bathurst (2005, 2006)) and 71 kPa (the load from the static and centrifugal force over the width of the plate) at the top and bottom of each backfill layer (similar to Ehrlich and Mirmoradi, (2015)). After considering the vibratory plate compactor load, the behavior of full-scale MSE walls was also studied under the dynamic load of a roller compactor.

This paper presents the results of an investigation to characterize the plate and roller compactors induced stress-strain response in MSE walls. The focus of this study is on the compaction process with plate compactor and on the assessment of fully compacted soil itself under the vibratory roller compactor. The intent is to model the plate and roller compactor effects in the soil pressures and reinforcement tensile forces measured in two full-scale MSE walls constructed with two different facing panels, using numerical analysis. Stress and strain sensors were placed at multiple depths between and over the reinforcement layers. Stress-strain behavior was also measured under the localized vibrating roller compactor load (Dynapac CA302) over a range of typical excitation force frequencies and amplitudes. The measurements of reinforcement's loads and strains, at full scale with both compaction and confining loads are instrumental in analyzing the behavior of MSE walls and can improve the accuracy of the design methods for reinforced earth structures.

2. FULL SCALE AND NUMERICAL MODELS

2.1 Preparing the models

In this study, the full-scale laboratory test results (two mechanically stabilized earth walls, one with full height plywood and one with full height concrete facing) are compared with the results of 2D numerical analysis. The instrumentation and configuration of the walls are shown in Figure 2a. The physical model was 4 m high, 3 m long and 4 m wide. The backfill soil in the test condition was compacted in layers prior to the dynamic test with using a vibrating plate (Ammann AVP 5920). The material was compacted to a relative density of 95.8% with an optimum water content of 12.4%, corresponding to a unit weight of 17.3 kN/m^3. The horizontal pressure was measured at different locations from the facing panel (a=0.05, 0.38, 0.71 and 1.04 m). Additionally, the vibratory roller compactor load (Dynapac CA302) with parameters presented in Table 1, was applied over the backfill in the area shown in Figure 2a after finishing the backfill construction. The strain gauges on the reinforcement layers are at; a=0.08, 0.32, 0.56, 0.8 and 1.04 m from the facing panel.

The numerical modeling was carried out using the two-dimensional finite-element program, Plaxis (Brinkgreve and Vermeer, 2002). In the 2D analysis, plane strain conditions and 15-node triangular elements with a fine mesh were used. To get more accurate results and minimizing the effect of the mesh size on the system, the mesh was refined around the reinforcement layers, roller compactor load and facing panel (Figure 2b). For the roller compactor, the harmonic load with the same frequency of real condition and the dynamic load magnitude of 180 kPa were used in the simulation. One, two, three and five cycles with the dynamic time intervals of 0.0303, 0.0606, 0.0909 and 0.1515 second are used in this study to simulate the dynamic behavior of the roller compactor after finishing the backfill construction step. The Plaxis hardening soil model with small-strain stiffness (HS-small) was applied for the numerical analysis.

Table 1. Roller compactor parameters.

Parameter	**Value**
Drum width (m)	2.13
Drum radius (m)	1.54
Static linear load (kN)	81
Operating frequency (Hz)	30
Centrifugal Force (kN)	146-300

Secant modulus E_{50}^{ref} and young's modulus for unloading and reloading E_{ur}^{ref} are determined from a triaxial stress-strain-curve. Absorbent boundaries around the model were assigned to the model to absorb stress waves without rebounding into the soil body. Rayleigh parameters are automatically calculated by the program after considering the 5% of material damping with the frequency of compactor. The model has an average element size of 0.15 m and in total 3795 elements. Kuhlemeyer and Lysmer (1973) suggest to assume a size less than or equal to one-eighth of the wavelength associated with the maximum frequency component f_{max} of the input wave:

$$\text{Average element size} \leq \frac{\lambda}{8} = \frac{V_{s,min}}{8 f_{max}} \quad (1)$$

where $v_{s,min}$ is the lowest wave velocity.

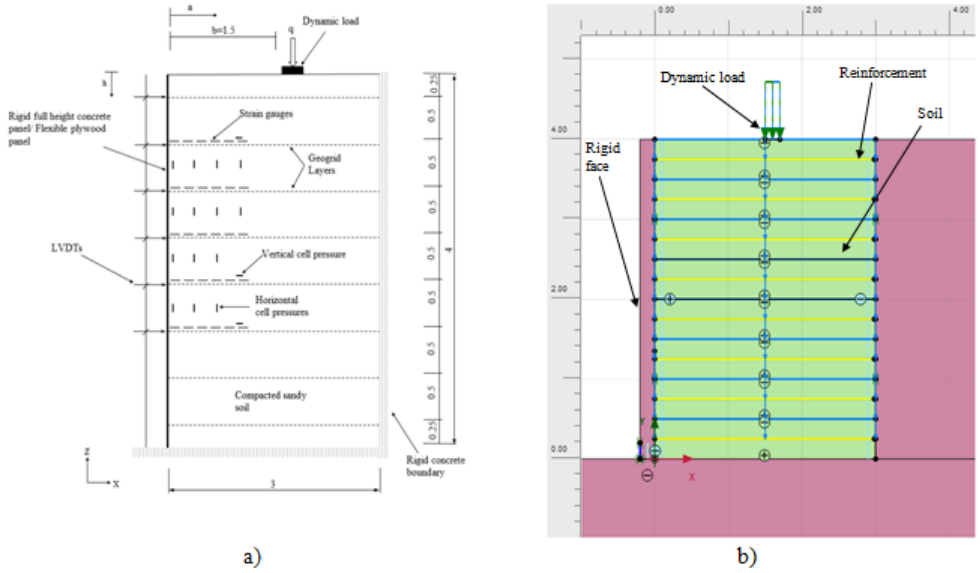

Figure 2. Models layout; a) full scale models and instruments (all dimensions are in m), b) 2D numerical model with concrete material around the backfill and for the wall face.

Plaxis automatically calculates the proper number of steps and sub steps from the considered time interval. The automatic procedure implemented in Plaxis ensures that a wave does not cross more than one element per time step. Further details of the experimental and numerical models can be found in Table 2. Maximum strains in the GR measured during backfill construction was limited to 0.5%. In this study long term condition (1000 hour) was considered for the GR (in numerical and experimental analysis). The stiffness of the GR was measured in accordance with DIN EN ISO 10319:2008 with considering the short term and long-term loading conditions. The geogrid reinforcement (GR) was modeled as a linear elastic material and with a reinforcement-soil interface friction angle equal to the soil friction angle. Rowe and Ho (1998) considered the perfect adherence as a reasonable assumption for the soil-geogrid interface friction coefficient ($\delta_{s,r}$=1) in their numerical analysis. In the analysis described in this paper, the reinforced concrete wall was assumed to be a linearly-elastic material with a modulus of elasticity of 3.5E7 KN/m^2 and a Poisson's ratio of 0.2 (from Damians et.al, 2013 and Miyata and Bathurst, 2007). This allows to model correctly the base condition of the rigid wall face. Under the base of the wall, the friction angle coefficient of the rough concrete-concrete is applied by using an interface element in the 2D numerical analysis. Soil layers were 'placed' every 0.25 m and 'compacted' until the final wall height was achieved. For modeling the compaction effect in every new layer of backfill, a temporary uniform load with 16 kPa has been applied only to the top (in the first model) and 71 kPa to the top and bottom (in the second model) of each backfill layer.

Table 2: Input parameters for Plaxis analysis.

Parameter	**Symbol**	**Value**
Wall height (m)	H	4
Unit weight-soil (kN/m^3)	γ_s	17.3
Reinforcement length (m)	L	3
Vertical spacing of reinforcement (m)	Sv	0.25 and 0.5
Long term (1000 hour) stiffness of reinforcements ($\varepsilon \leq 0.5\%$) (kN/m)	EA	670
short term (1 hour) stiffness of reinforcements ($\varepsilon \leq 1\%$) (KN/m)	EA	770
Young's modulus for unloading and reloading (kN/m^2)	E_{ur}^{ref}	112000
Secant modulus (kN/m^2)	E_{50}^{ref}	42500
Tangent stiffness (kN/m^2)	E_{oed}^{ref}	38500
Power	M	0.5
Failure ratio	R_f	0.74
Soil Poisson's ratio	ν_s	0.3
Concrete and plywood wall bending stiffness (kNm^2/m)	EI	23.3E3, 66.6
Concrete and plywood wall normal stiffness (kN/m)	EA	7.0E6, 5E5
Estimated soil plane strain friction angle (Wroth [28]) (º)	φ_{ps}	44
Peak soil friction angle from the triaxial test (º)	φ_{tx}	39.09
Residual friction angle from the triaxial test (º)	φ_r	35.15
Soil dilation angle from the test (º)	Ψ	12.5
Soil to nylon coefficient of friction angle (º)	φ_{sw}	11.5
Soil-reinforcement friction angle coefficient	$\delta_{s,r}$	1
Soil-concrete friction angle coefficient	$\delta_{s,c}$	0.55
Rough concrete-concrete friction angle coefficient	$\delta_{c,c}$	0.95
Soil-wood friction angle coefficient	$\delta_{s,w}$	0.45
Concrete young's modulus (kN/m^2)	E_c	2.1E8
Cohesion-soil (kPa)	C	1*
Shear modulus at small strains (kN/m^2)	G_0	155000
Shear strain at which G has reduced to 70% of G_0	$\gamma_{0.7}$	2E-4

*due to the moisture content (12.4%), there will be some cohesion.

2.2 Vertical earth pressure

Figure 3a and b show the vertical earth pressure distribution in test and numerical analysis, before and after the roller dynamic load. For both the flexible and rigid face, the dimensionless vertical earth pressure coefficient as found in the tests is compared with the Plaxis analysis in these figures. Different dynamic time intervals (one, two, three and five cycles) were considered in the numerical analysis. There is good agreement between tests and numerical analysis in cell pressures located in different positions in these figures. In Figure 3b, for the rigid (concrete) face, the vertical stresses were smaller than the geostatic line, while for the flexible (wooden) face, the stresses were higher until the bottom (1.75m) of the wall. In both tests the distribution is not linear with depth, and had a maximum value at a height of 1.75 m. Abu-Hejleh et al. (2001), Caroll and Richardson (1986) and Bathurst et al. (1993) also reported measured pressures that were smaller than the calculated ones.

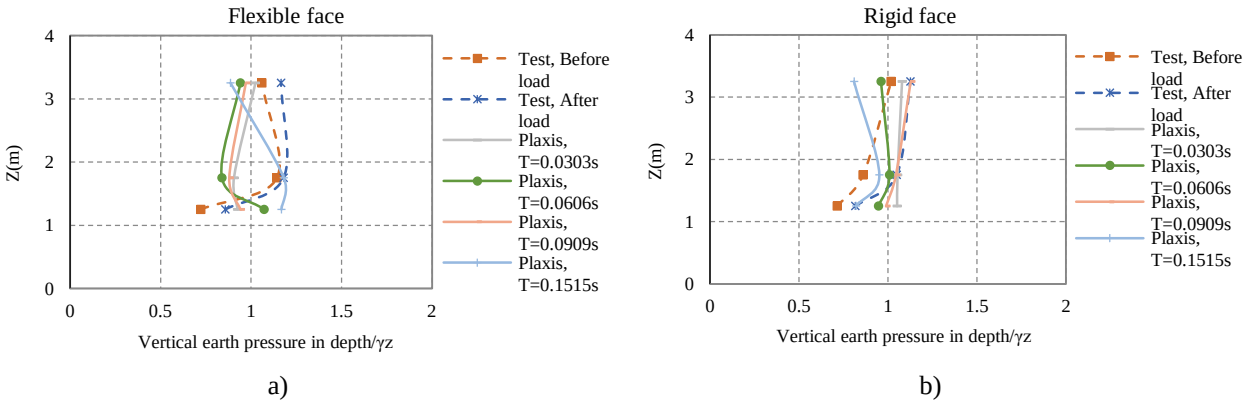

Figure 3. Vertical earth pressure distribution before and after roller dynamic load; a) flexible face, b) rigid face.

2.3 Lateral earth pressure coefficient

Figure 4 indicates the normalized values of the horizontal soil stress measured through the cell pressures placed at different positions from the walls after the backfill construction. For normalization, the values were divided by γh to obtain the lateral earth pressure coefficient K. The horizontal lines in these plots represent the active lateral earth pressure coefficient, K_a, and the original horizontal stress K_0 in the reinforced soil mass after the backfill construction.

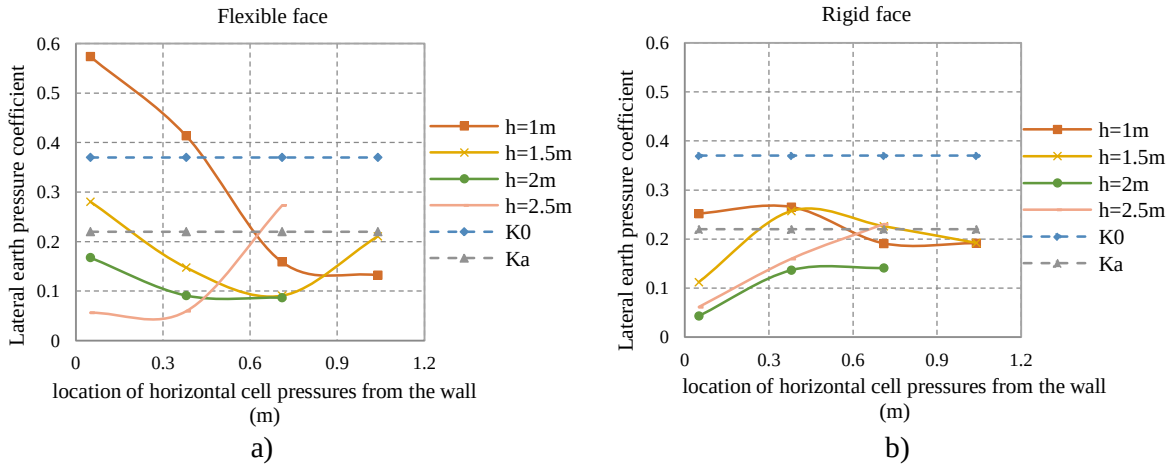

Figure 4. Lateral earth pressure coefficient after backfill construction step in full-scale tests; a) flexible face, b) rigid face.

This normalization shows that for cell pressures located far from the face, the K value is lower than the

K_a (using the Rankine theory) in both the flexible and the rigid face. The lateral earth pressure reduction can occur because the vertical stress close to the wall is less than γh due to friction effects with the wall (Coulomb, 1776) or by the friction between the soil and the reinforcement layers in the horizontal direction (Ruiken et al., 2010). For the upper cell pressure and close to the flexible face, the K value is more than the K_0 and shows the compaction effect in the upper parts. On the other hand, in the rigid face, the K value is close to the K_a in upper cell pressures. From these figures, the influence of the compaction load on K in the upper layers is larger than in the lower layers. This shows that when the compaction load is less than the geostatic stress, the effects of the induced stresses due to compaction decrease (Mirmoradi and Ehrlich, 2014). The influence of compaction is more pronounced in the flexible than the rigid face and this shows that compaction load effects in depth can also change due to the facing panel rigidity. For the flexible face, the K value is close to K_0 in the lower layer (h=1.5m). Figure 5 shows the results of numerical analysis for the lateral earth pressure coefficient at different depths and with different compaction loads for the backfill construction step. A single load-unload stress cycle with 16 kPa (type 1) and 71 kPa at the top and bottom of each backfill layer (type 2) were used to model the compaction process in these figures. From Figure 5a and b, the influence of the small compaction load (16 kPa) in the upper layers is less than the geostatic stress effect in the lower layers. In these figures, the K value is mostly located between the K_0 and K_a. In Figure 5c and d, the compaction load (71 kPa) has the same influence on the upper and lower layers. For the rigid and flexible face, the K value in the soil is mostly located between the K_0 and K_a.

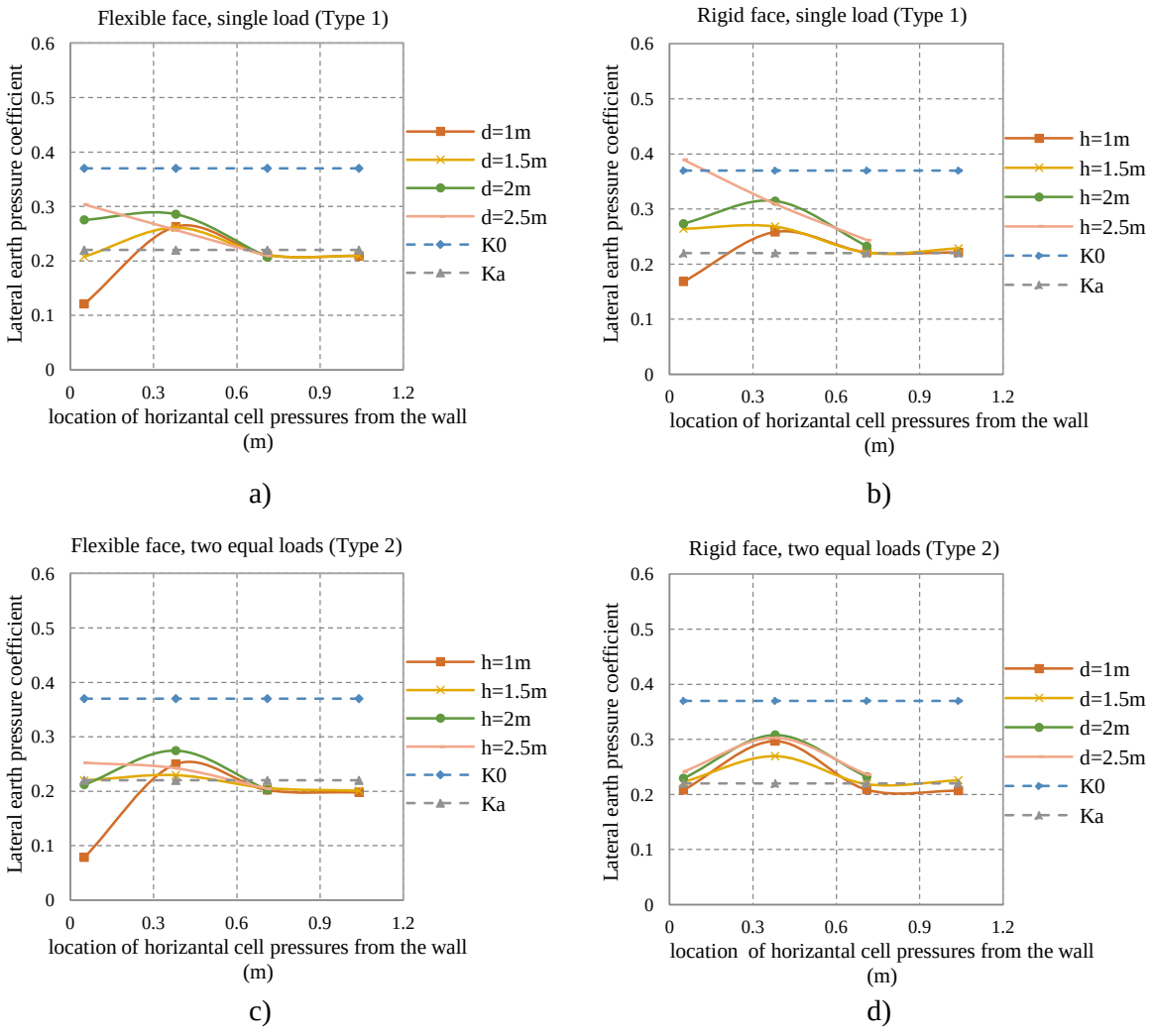

Figure 5. Lateral earth pressure coefficient after backfill construction step in numerical analysis; a and b) with single load (16 kPa), c and d) with two equal loads (71kPa).

By comparing the test results with the numerical analysis in Figure 4 and Figure 5, there is reasonable agreement between the second method (71 kPa at the top and bottom of each backfill layer) and test results in rigid face. For the flexible face, there is still a discrepancy between the numerical analysis and the test results especially for points close to the face and upper layers. This discrepancy is larger for the second method than the first method.

Figure 6 shows the measured lateral cell pressure coefficients after the dynamic roller compactor load in full-scale tests. In comparison with Figure 4, for the flexible face, two layers of pressure cells (that were in h=1m and 1.5m) have a value more than the K_0 and for the pressure cells close to the face, the K value decreased after the roller compaction load. By increasing the distance of the cell pressures from the flexible face in these layers, the K value increases to almost two times the K_0 value. In deeper cell pressure layers (h=2m and 2.5m), the measured values are under the K_a line. In the rigid face, for cell pressures in the first layer (h=1m) and close to the face and to the dynamic load, the value is more than the K_0. For this layer, there is minimum value in the middle. The other cell pressures located near the rigid face in deeper layers, have the value close to the K_a line that shows the increment in K value compared to the Figure 4. From these figures, the compaction has more influence in the lateral earth pressure coefficient for the flexible wall than for the rigid wall and the influence is more for the upper parts than the deeper.

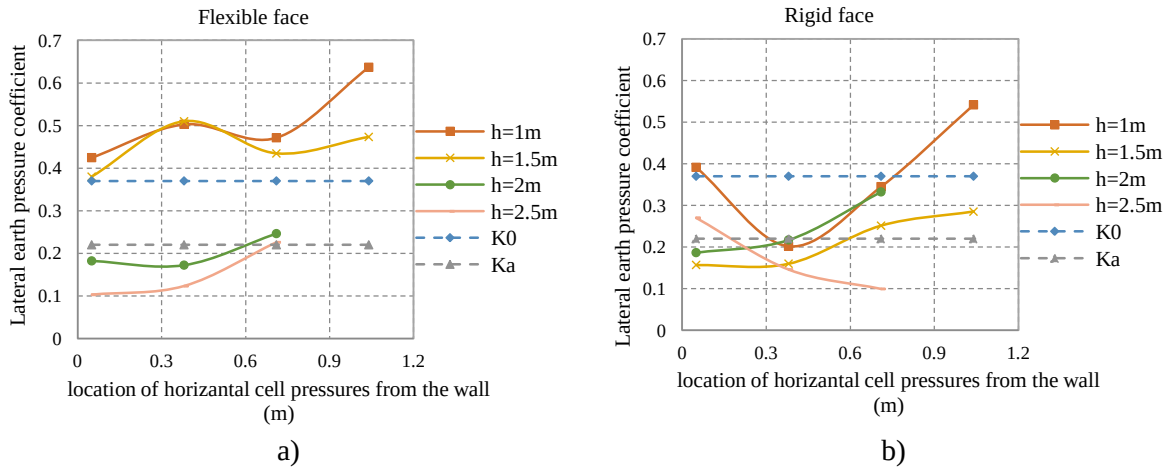

Figure 6. Lateral earth pressure coefficient after dynamic roller compactor load; a) flexible face, b) rigid face.

Figure 7 shows results of the numerical analysis for lateral earth pressure coefficient at different depths and under the dynamic roller compactor load (after the backfill construction step). For normalization, the values were divided by γh. Different dynamic time intervals (with one, two, three and five cycles) were considered in the numerical analysis for comparison to simulate the dynamic behavior in different cycles. For the dynamic load with T=0.0303s in Figure 7a and b, the calculated K values are close to the K_a line, apart from the first layer in the rigid face. In this figure, the first layer has a higher value than the other layers for the flexible and rigid face. In Figure 7c and d with T=0.0606s (two cycles), the maximum K value decreases by increasing the depth. In the rigid and flexible walls, the first layer (h=1m) has a K value bigger than the K_0 and the deeper layers have value less than the K_0. By increasing the dynamic time interval to T=0.0909s (three cycles) in Figure 7e and f, the K value increases to more than the K_0 value near the dynamic load in the rigid and flexible face. Similar to the test results, there is an optimum K value in the first layer for the rigid face and the difference between the K value in first layer and deeper layers is less compared to the test results. In Figure 7g and h, the calculated K value with T=0.1515s (five cycles) are compared with K_0 and K_a in flexible and rigid face. For the first layer of cell pressures (h=1m), the calculated K value in flexible face is more than the rigid face. By increasing the depth, the K value for the rigid face is increasing more than flexible face. In comparison with test results (Figure 6), the numerical analysis with this dynamic time interval showed more lateral earth pressure under the dynamic compaction load.

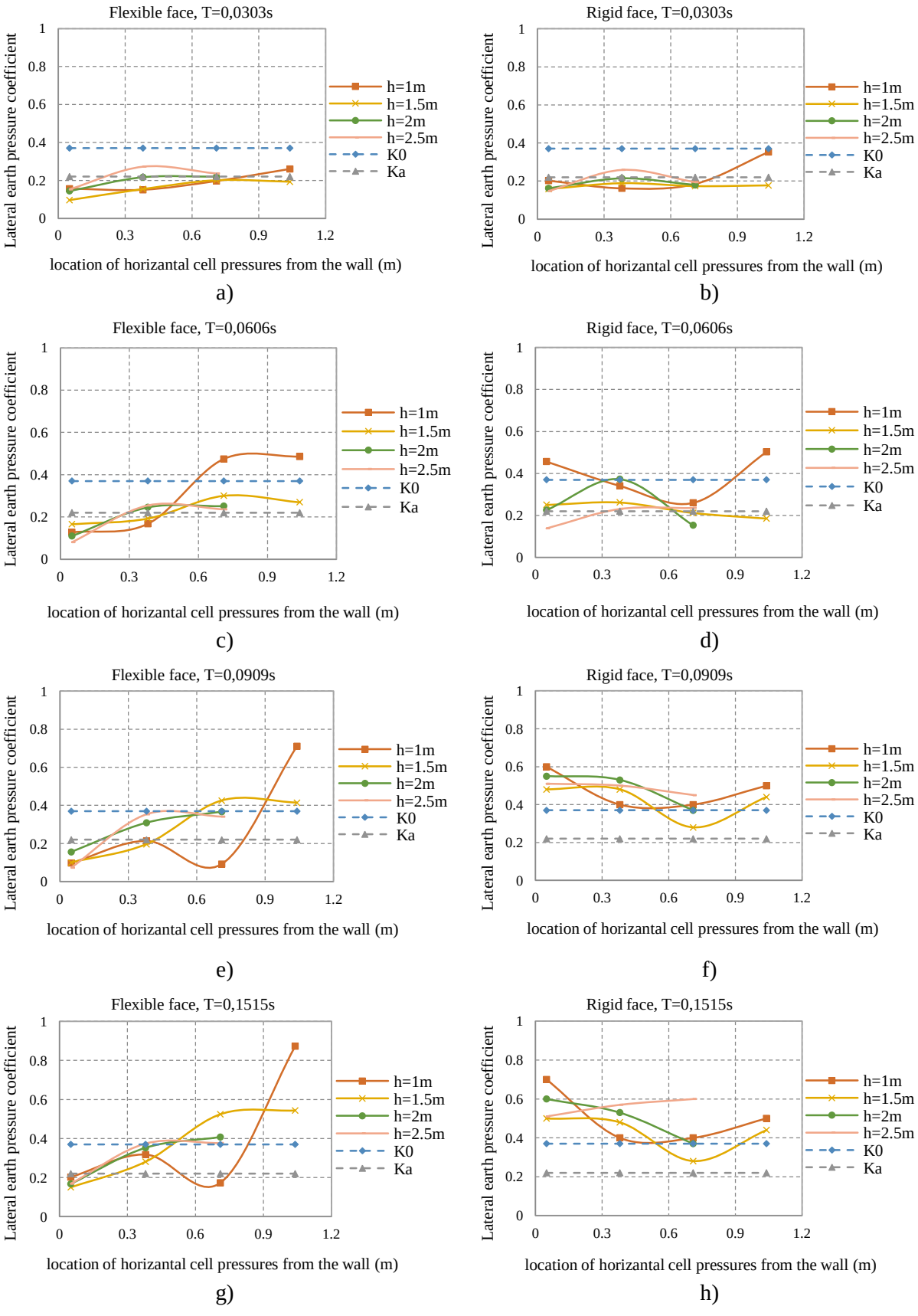

Figure 7. Lateral earth pressure coefficient after the roller compactor load, flexible face and rigid face; a and b) T=0.0303s, c and d) T=0.0606s, e and f) T=0.0909s, g and h) T=0.1515s.

3. MAXIMUM TENSILE FORCES

Figure 8a shows the maximum tensile load on reinforcement layers from the measured and 2D numerical analysis after the backfill construction step. The long term (1000 hour) stiffness of the geogrid is used for determining the maximum tensile forces in the reinforcement layers. In this figure, there is a small difference between the numerical analysis, considering the equal loads on top and bottom of each backfill layer and the test results.

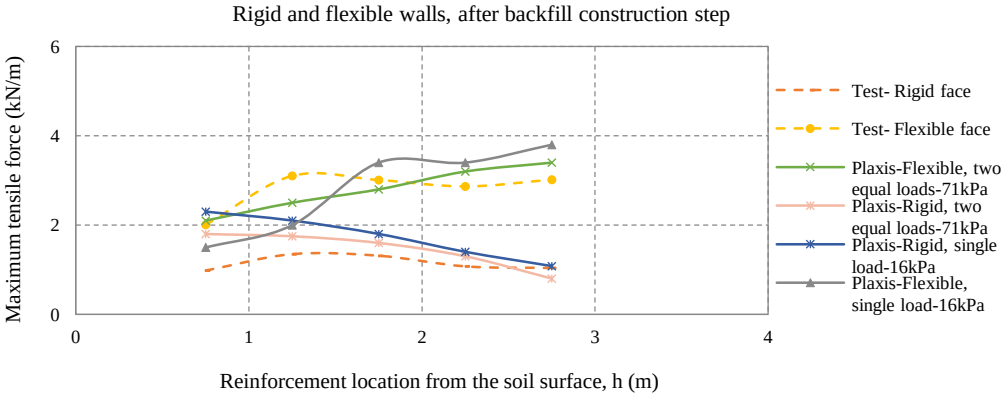

a)

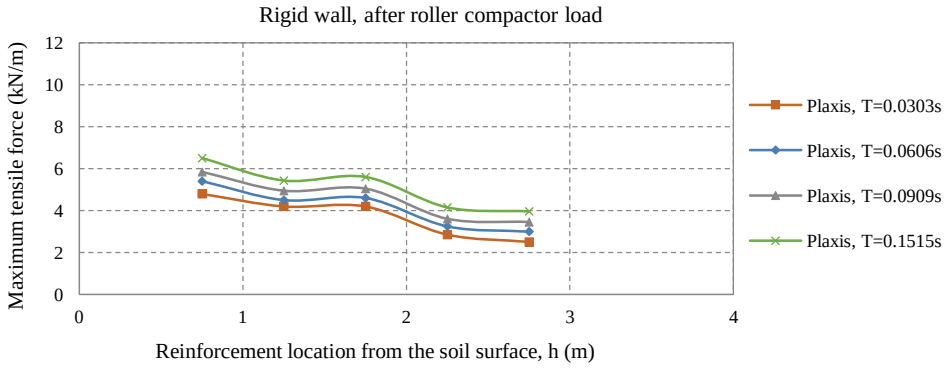

b)

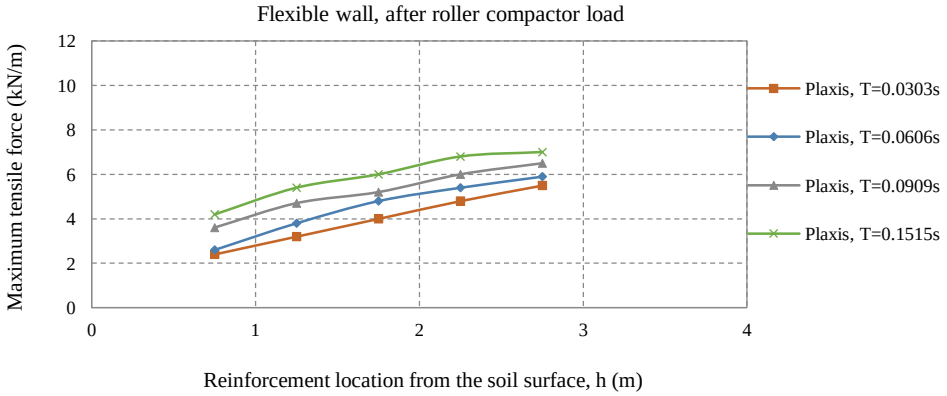

c)

Figure 8. Maximum tensile loads on reinforcement layers in measurement and Plaxis analysis; a) after backfill construction step, b and c) after applying the dynamic roller compactor load.

The difference between the test results and the numerical analysis in this figure increases with depth for the flexible face and decreases for the rigid face by considering only a distributed load on top of the backfill soil layers. This maximum tensile force in the flexible wall is larger than the rigid face for test and numerical analysis. In Figure 8b and c, the maximum measured tensile loads in the reinforcement layers after applying the roller compactor load are compared in numerical results considering different dynamic time intervals (one, two, three and five cycles) in flexible and rigid walls. From these figures, by increasing the dynamic time interval, the calculated maximum tensile load distribution is increasing in flexible and rigid walls. In flexible wall, the maximum load increases by increasing the depth but for the rigid wall the direction is opposite and the load decreases by the depth.

4. CONCLUSIONS

Results of large scale model tests are presented on geogrid reinforced walls loaded with a large roller compactor. The measurements are compared with the results of the numerical analysis in the vertical and horizontal earth pressures, maximum tensile forces in reinforcement layers after backfill construction step and roller dynamic compactor load. For MSE walls, compaction load influences the lateral earth pressure and consequently maximum tensile force in the reinforcement layers.

The instrumentation used in this study provided valuable measurements of strains in the reinforcements, vertical and lateral earth pressure before and after applying the dynamic roller compactor load. These results illustrate the effect of facing panel properties on the related system behavior. Furthermore, the more rigid concrete facing panel has the maximum tensile force on a higher point on the wall than the flexible wall. This causes a deeper failure zone for the flexible face after applying the dynamic roller compactor load than for the rigid face. It also shows that for the rigid face compared to the flexible face, upper layers have more influence on the stability and wall deflection.

By increasing the flexural rigidity of the facing panel, the reinforcement strains decrease in the numerical simulation, as was also found in the measurements.

There is good agreement between the numerical analysis and experimental results for the maximum tensile loads for both the rigid and the flexible wall by considering two equal distributed loads in top and bottom of each soil layer in backfill construction step.

5. ACKNOWLEDGMENTS

The authors appreciate the help of the Iranian Ministry of Science, Research and Technology for financial support and the NAUE Company for supplying the measurements.

6. REFERENCES

Abu-Hejleh N, Zornberg J, Wang T, McMullen M, Outcalt W (2001). Performance of Geosynthetic-Reinforced Walls Supporting the Founders/Meadows Bridge and Approaching Roadway Structures, Report 2: Assessment of the Performance and Design of the Front GRS Walls and Recommendations for Future GRS Abutments, Report No. CDOT-DTD-R-2001-12, *Colorado Department of Transportation, Colorado, USA*, 143 p.

Anderegg R, Kaufmann K (2004). Intelligent compaction with vibratory rollers. *Transportation Research Record. 1868, Transportation Research Board, Washington, D.C*, 124–134.

Bathurst RJ, Simac MR, Cristopher BR, Bonczkiewicz C (1993). Database of Results from a Geosynthetic Reinforced Modular Block Soil Retaining Wall, *Proceedings of Soil Reinforcement: Full Scaie Experiments of the 1980ts, ISSMFEIENPC, Paris, France, November 1993*, pp. 341-365.

Bathurst RJ, Nernheim A, Walters DL, Allen TM, Burgess P, Saunders DD (2009). Influence of reinforcement stiffness and compaction on the performance of four geosynthetic reinforced soil walls. *Geosynth. Int.* 16 (1), 43e59.

Bell FG (1993). Engineering Treatment of Soils. *E&FN Spon, London*.

Brinkgreve RBJ, Vermeer PA (2002). Plaxis: Finite Element Code for Soil and Rock Analyses, *version 8," Balkema*.

Caroll RG, Richardson GN (1986). Geosynthetic reinforced retaining walls. *Proceedings of the Third International Conference on Geotextiles*, Vienna, Austria.

Coulomb CA (1776). Essai sur une application des regles de maximis et minimis a quelqes problemas de stratique relatifs a l'architecture. Memoires de mathematique et de physique. Presentes a l'Academie Royale des Sciences, Paris 7, pp. 343-382.

Damians IP, Bathurst RJ, Josa A, Lloret A, Albuquerque PJR (2013). Vertical facing loads in steel reinforced soil walls. *J Geotech Geoenviron Eng (ASCE)*; 139(9):1419–32.

DIN, Geotextiles-Wide width tensile test (DIN EN ISO 10319:2008). Deutsches Institut für Normung e.V.

Ehrlich M, Mitchell JK (1995). Working stress design method for reinforced soil walls. Closure. *J. Geotech. Eng. ASCE* 121 (11), 820e821.

Ehrlich M, Mirmoradi SH (2013). Evaluation of the effects of facing stiffness and toe resistance on the behavior of GRS walls, *Geotext. Geomembr*, 40, 28-36.

Gotteland Ph, Gourc JP, Jommi C, Nova R (1996). Finite difference analysis of geotextile reinforced earth walls. *In Proceedings of EuroGeo 1*, the 1st European Geosynthetics Conference, Maastricht, the Netherlands. pp. 503–510.

Hatami K, Bathurst RJ (2005). Development and verification of a numerical model for the analysis of geosynthetic reinforced soil segmental walls under working stress conditions. *Canadian Geotechnical Journal.*, 42(4): 1066-1085.

Hatami K, Bathurst RJ (2006). Numerical model for reinforced soil segmental walls under surcharge loading. *ASCE Journal of Geotechnical and Geoenvironmental Engineering*, 132(6): 673-684.

Huang B, Bathurst RJ, Hatami K (2009). Numerical study of reinforced soil segmental walls using three different constitutive soil models. *ASCE Journal of Geotechnical and Geoenvironmental Engineering*, 135(10): 1486-1498.

Kröber W, Floss R, Wallrath W (2001). Dynamic soil stiffness as quality criterion for soil compaction. *Geotechnics for roads, rail tracks, and earth structures*, Balkema, Lisse.

Kuhlemeyer R, Lysmer J (1973). Finite Element Method Accuracy for Wave Propagation Problems. *Journal of the Soil Dynamics Division*, 99, 421-427.

Mirmoradi SH, Ehrlich M (2014). Modeling of the compaction-induced stresses in numerical analyses of GRS walls. *International Journal of Computational Methods* (IJCM), Special Issue on Computational Geomechanics.

Mirmoradi SH, Ehrlich M (2015). Modeling of the compaction-induced stress on reinforced soil walls. *J. Geotext. Geomembr*, 43 (1), pp. 82–88.

Miyata Y, Bathurst RJ (2007). Evaluation of K-Stiffness method for vertical geosynthetic 480 reinforced granular soil walls in Japan. *Soils and Foundations*, 47, No. 2, 319–335.

Mooney MA, Rinehart RR (2007). Field Monitoring of Roller Vibration during Compaction of Subgrade Soil.

J. Geotech. & Geoenviron. Engineering, ASCE, 133(2), 257-265.

Riccio M, Ehrlich M, Dias D (2014). Field monitoring and analyses of the response of a block-faced geogrid wall using fine-grained tropical soils. *Geotext. Geomembr*. 42 (2), 127e138.

Rowe RK, Ho SK (1998). Horizontal deformation in reinforced soil walls. *Canadian Geotechnical Journal.*, Vol. 35, No. 2, pp. 312-327.

Ruiken A, Ziegler M, Vollmert L, Duzic I (2010). Recent findings about the confining effects of geogrids from large scale laboratory testing. 9th International Conference on Geosynthetics, Brazil.

Tatsuoka F, Uchimura T, Tateyama M (1997). Preloaded and pre-stressed reinforced soil. *Soils Found*. 37 (3), 79e94.

Toombes AF (1969). The Performance of an Aveling Barford VP 7.7 Mg Self-propelled Vibrating Roller in the Compaction of Soil. *Transport and Road Research Laboratory*, Report LR257, Crowthorne.

Uchimura T, Tateyama M, Tanaka I, Tatsuoka F (2003). Performance of a preloaded-prestressed geogrid-reinforced soil pier for a railway bridge. *Soils Found.* 43 (6), 155e171.

Wroth CP (1984). The interpretation of in situ soil tests. 24th Rankine Lecture, *Géotechnique* 34, No. 4, pp 449-489.